

## SOLAR CELLS

# Spontaneous formation of robust two-dimensional perovskite phases

Shaun Tan<sup>1†</sup>, Meng-Chen Shih<sup>1†</sup>, Yongli Lu<sup>1†</sup>, Seung-Gu Choi<sup>2</sup>, Yifan Dong<sup>3</sup>, Joo-Hong Lee<sup>2</sup>, Ilhan Yavuz<sup>4</sup>, Bryon W. Larson<sup>3</sup>, So Yeon Park<sup>3</sup>, Tim Kodalle<sup>5,6</sup>, Ruiqi Zhang<sup>7</sup>, Matthias J. Grotevent<sup>1</sup>, Yu-Kuan Lin<sup>1</sup>, Hua Zhu<sup>1</sup>, Vladimir Bulović<sup>7</sup>, Carolin M. Sutter-Fella<sup>5</sup>, Nam-Gyu Park<sup>8,9</sup>, Matthew C. Beard<sup>3</sup>, Jin-Wook Lee<sup>2,9</sup>, Kai Zhu<sup>3\*</sup>, Moungi G. Bawendi<sup>1\*</sup>

The two-dimensional on three-dimensional (2D/3D) perovskite bilayer heterostructure can improve the stability and performance of perovskite solar cells. We show that the 2D/3D perovskite stack in a device evolves dynamically during its end-of-life decomposition. Initially phase-pure 2D interlayers can evolve differently, resulting in different device stabilities. We show that a robust 2D interlayer can be formed using mixed solvents to regulate its crystallinity and phase purity. The resulting 2D/3D devices achieved 25.9% efficiency and had good durability, retaining 91% of their initial performance after 1074 hours at 85°C using maximum power point tracking.

The development of two-dimensional on three-dimensional (2D/3D) perovskite bilayer heterostructures has helped boost the performance and durability of perovskite solar cells (PSCs) (1–8). The 2D interlayer can passivate defects, control charge transport, create a built-in potential, prevent external ingress from the environment, and block ion migration (1–8). However, for these advantages to be retained, the 2D interlayer needs to be stable; the 2D interlayer must not evolve structurally or compositionally to become nonfunctional. In this work, we show that 2D interlayers can evolve dynamically during device aging and that phase-pure 2D interlayers (9) can undergo different evolution pathways. We also demonstrate how excess PbI<sub>2</sub> can facilitate 2D formation to promote phase-purity and crystallinity.

We investigated the changes that can occur to 2D perovskite interlayers during long-term illumination. We aged our baseline control 2D/3D device under full-spectrum 1-sun illumination with ultraviolet (UV) included in a nitrogen atmosphere. The 3D perovskite was a FAPbI<sub>3</sub>-based composition (FA, formamidinium) with added MA(Cl) and MAPbBr<sub>3</sub> (MA, methylammonium) for improved crystallization (10, 11) as well as excess PbI<sub>2</sub>. The excess PbI<sub>2</sub> has several roles that will be discussed throughout this work. All devices are based on the n-i-p structure with SnO<sub>2</sub> and 2,2',7,7'-Tetrakis[N,N-di(4-methoxyphenyl)amino]-9,9'-spirobifluorene (spiro-MeOTAD) as the charge transporting layers. Under maximum power point (MPP) tracking, the control 2D/3D device had poor photostability (fig. S1), where 74% of its initial performance was maintained after 500 hours.

We used coupled-geometry x-ray diffraction (XRD) with sufficient penetration depth to probe the buried 2D interlayer in a device stack. Specifically for the control 2D/3D device (fig. S2), the initial  $n = 2$  quasi-2D perovskite phase [L<sub>2</sub>APb<sub>2</sub>X<sub>7</sub>, hereafter referred to as 2D ( $n = 2$ ), where L, A, and X refer to the spacer organic ligand octylammonium (Oc), the A-site organic cation, and halide anion, respectively, and  $n$  refers to the PbX<sub>6</sub> octahedra layer number] gradually disappeared, with partial transformation into PbI<sub>2</sub> and the  $n = 1$  2D phase [L<sub>2</sub>PbX<sub>4</sub>, referred to as 2D ( $n = 1$ )]. We postulated that the poor device stability under MPP tracking was related to this disappearance of most of the 2D interlayer. The bare 3D device had low power conversion efficiency (PCE) because of abundant unpassivated defects. With the loss of most of the 2D interlayer, the 2D/3D device lost its defect passivation and essentially reverted back to behave like a bare 3D device. The PCE decreased through degradation because the 2D/3D device slowly turned into a bare 3D device. This degradation process was also evident in the changes of their carrier lifetimes before and after illumination (fig. S3). Additionally, the bare 3D device underwent severe initial decay. This so-called burn-in decay was caused by rapid defect migration (12–14). As the 2D interlayer disappeared with time, defect migration occurred over a longer duration. The burn-in was not rapid but became an extended period degradation of the 2D/3D device. Overall, the control 2D/3D device was not stable, and most of the 2D perovskite layer disappeared under illumination (discussion in supplementary text S1). These findings motivated us to create a durable 2D interlayer.

## 2D interlayer formation studies

We used time-resolved, *in situ* grazing-incidence wide-angle x-ray scattering (GIWAXS) to study the formation dynamics of 2D/3D perovskites. Hereafter, the phases present initially upon deposition, excluding the 3D perovskite, are referred to as the initial phase. The previously discussed control 2D/3D perovskites are labeled as the Oc films. The initial phase consisted of the 2D ( $n = 1$ ) perovskite and unreacted PbI<sub>2</sub> (Fig. 1, A and B, and fig. S4A). The PbI<sub>2</sub> peak subsequently weakened when the annealing of the film began, but this PbI<sub>2</sub> was not fully consumed and was residual in the final film. The 2D ( $n = 1$ ) perovskite only partially converted into the 2D ( $n = 2$ ) phase, so the final film contained an impure mixture of 2D ( $n = 1$ ), 2D ( $n = 2$ ), and PbI<sub>2</sub> phases. Further experiments indicate that the excess PbI<sub>2</sub> in the 3D perovskite composition facilitated 2D formation by providing a readily available PbI<sub>2</sub> source (fig. S5) but with the disadvantage that unreacted PbI<sub>2</sub> would remain. For the 3D phase with no excess composition, although no unreacted PbI<sub>2</sub> remained, the 2D perovskite phase had low crystallinity, and the PCE was poor (fig. S6; supplementary text S2). This trade-off presented an opportunity to assess the interplay between 2D perovskite crystallinity and residual PbI<sub>2</sub>.

Unless otherwise stated, all 2D/3D perovskites were based on the 3D with excess PbI<sub>2</sub> composition. Utilizing mixed solvent systems with MA led to a stepwise progression to promote formation of the 2D ( $n = 2$ ) phase. First, Oc ligand with MA additive in isopropanol (IPA) (OcMA) formed a 2D ( $n = 1$ ) initial phase (Fig. 1, C and D), which converted into the 2D ( $n = 2$ ) phase upon annealing. PbI<sub>2</sub> and 2D ( $n = 1$ ) were fully reacted, unlike in the control Oc film. Next, the initial phase formed with OcMA with mixed dimethylformamide and IPA (OcMA:F) consisted of a multiphase mixture of 2D ( $n = 1$ ) and 2D ( $n = 2$ ), and the 2D ( $n = 1$ ) fully converted into 2D ( $n = 2$ ) in the final film (Fig. 1, E and F). Lastly, for OcMA with mixed dimethyl sulfoxide and IPA (OcMA:S), the 2D ( $n = 2$ ) perovskite now became the equilibrium phase, forming spontaneously (Fig. 1, G and H, and fig. S7); neither PbI<sub>2</sub> nor 2D ( $n = 1$ ) nor any other secondary by-products were present. Despite the excess PbI<sub>2</sub> in the 3D perovskite composition, there was no unreacted PbI<sub>2</sub> left after 2D formation, and a phase-pure 2D perovskite formed with high crystallinity (Fig. II).

<sup>1</sup>Department of Chemistry, Massachusetts Institute of Technology (MIT), Cambridge, MA, USA. <sup>2</sup>Department of Nanoengineering and Department of Nano Science and Technology, SKKU Advanced Institute of Nanotechnology (SAINT), Sungkyunkwan University, Suwon, Republic of Korea. <sup>3</sup>Chemistry and Nanoscience Center, National Renewable Energy Laboratory (NREL), Golden, CO, USA. <sup>4</sup>Department of Physics, Marmara University, Ziverbey, Istanbul, Turkey. <sup>5</sup>Molecular Foundry, Lawrence Berkeley National Laboratory, Berkeley, CA, USA. <sup>6</sup>Advanced Light Source, Lawrence Berkeley National Laboratory, Berkeley, CA, USA. <sup>7</sup>Department of Electrical Engineering and Computer Science, MIT, Cambridge, MA, USA. <sup>8</sup>School of Chemical Engineering, Sungkyunkwan University, Suwon, Republic of Korea. <sup>9</sup>SKKU Institute of Energy Science & Technology (SIEST), Sungkyunkwan University, Suwon, Republic of Korea. \*Corresponding author. Email: kai.zhu@nrel.gov (K.Z.); mgb@mit.edu (M.G.B.) †These authors contributed equally to this work.

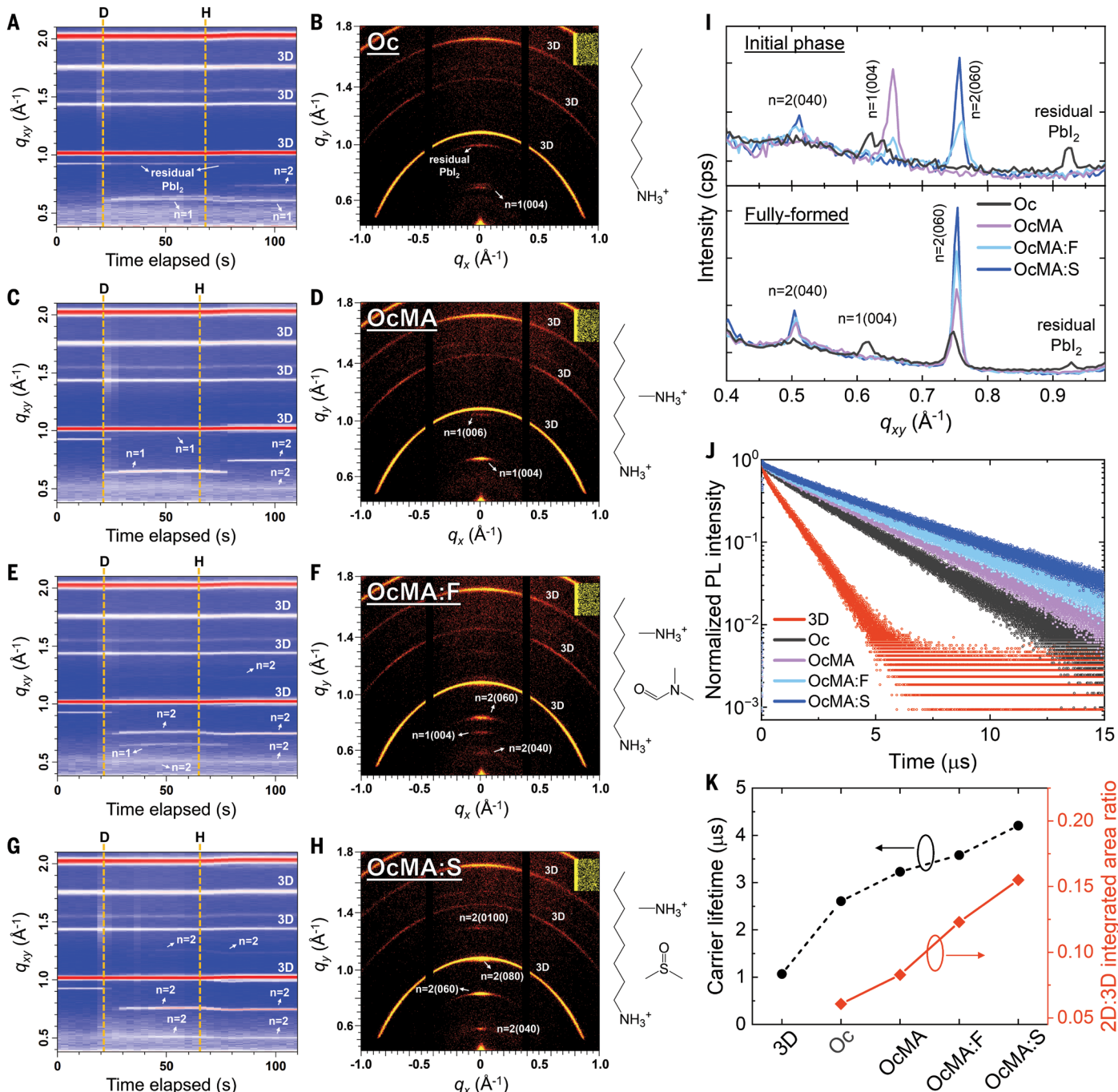


**Fig. 1. 2D perovskite formation and crystallinity.** (A to H) In situ GIWAXS measurements and initial phase GIWAXS patterns of the Oc [(A) and (B)], OcMA [(C) and (D)], OcMA:F [(E) and (F)], and OcMA:S [(G) and (H)] 2D/3D perovskites. Labels D and H denote the deposition time and annealing start time, respectively.  $q$ , scattering vector. (I) Azimuthal integrated GIWAXS patterns of the 2D/3D perovskites. Top and bottom panels respectively show the initial and final 2D phases. cps, counts per second. (J) Time-resolved photoluminescence (PL) spectra of the 2D/3D perovskites on glass. (K) Plot of carrier lifetime (in black) and 2D:3D integrated area ratio (in red) of the 2D/3D perovskites. The 2D:3D integrated ratio was calculated as the ratio of the 2D ( $n = 2$ ) (060) to 3D (001) integrated peak areas for the final 2D/3D perovskites.

OcMA, OcMA:F, and OcMA:S all attained a final phase-pure 2D ( $n = 2$ ) perovskite. This allowed us to exclude phase purity as a contributing factor when comparing their material properties. The final crystallinity of the 2D ( $n = 2$ ) phase increased in the order Oc < OcMA < OcMA:F < OcMA:S. This trend was consistent when evaluating the GIWAXS integrated peak area (Fig. II and fig. S8), full-width half-maximum

broadening, and Halder-Wagner analysis from lab-based grazing-incidence XRD of the 2D/3D perovskites (fig. S9). We observed a correlation between 2D crystallinity and carrier lifetime (Fig. 1, J and K). The bare 3D film had a carrier lifetime of 1067 ns, which increased by 244% to 2608 ns for the Oc film owing to defect passivation by the 2D interlayer. The unreacted  $\text{PbI}_2$  left over likely contributed to

the increased lifetime (15), convoluting with the 2D interlayer contribution. Regardless, the OcMA:S film, even with no unreacted PbI<sub>2</sub>, showed the longest carrier lifetime of 4205 ns (394% increase over the bare 3D film), demonstrating effective suppression of nonradiative recombination.

We extended our study to understand the 2D formation mechanisms (Fig. 2A and table S1). Different mixed solvents had varying consequences (fig. S10). For OcMA with methyl glycol and IPA (OcMA:MG) and OcMA with acetonitrile and IPA (OcMA:A), 2D crystallinity and formation were similar compared with that of (IPA only). Meanwhile, OcMA:F (Fig. 1E), OcMA with 1-methyl-2-pyrrolidone and IPA (OcMA:N), and OcMA with propylene carbonate and IPA (OcMA:PC) all formed a mixed 2D ( $n = 1$ ) and 2D ( $n = 2$ ) initial phase, with final 2D ( $n = 2$ ) crystallinity improved compared with that of OcMA. This also suggested OcMA:PC as a promising candidate, and the measured carrier lifetime of 3842 ns trended with 2D crystallinity (fig. S11). The mixed solvent and MA together synergistically regulated 2D formation. Without MA, Oc:S showed comparable crystallinity and formation relative to the control Oc (fig. S12). Without the mixed solvent and regardless of the MA halide choice, the final 2D ( $n = 2$ ) crystallinity was only slightly improved over that of the control Oc (fig. S13). In this work, only OcMA:S (Fig. 1G) spontaneously formed a 2D ( $n = 2$ ) initial phase and had the highest final 2D crystallinity. Lastly, increasing the MA concentration in OcMA:S showed the possibility of forming the higher-order 2D ( $n = 3$ ) phase (fig. S14).

Preliminary theoretical calculations helped shed light on the experimental observations (supplementary text S3 and tables S2 to S5). 2D formation involved partial dissolution of the 3D perovskite surface, followed by secondary recrystallization into the 2D phase (16–18). A stronger solvent interaction assisted with this dissolution (Fig. 2, B to E, and figs. S15 to S18), which was necessary to source the precursor components (PbI<sub>2</sub> and FA) from the 3D surface used for 2D formation. Sourcing of FA also led to the formation of a FA-based 2D ( $n = 2$ ) perovskite. The MA additive functioned to thermodynamically promote 2D ( $n = 2$ ) formation during its initial stage (fig. S19), followed by MA volatilization and FA substitution, resulting in a high-crystallinity FA-based 2D ( $n = 2$ ) phase (supplementary text S4, fig. S20, and table S6). This is akin to the role of MA to promote 3D perovskite intermediate phase crystallization (10, 19, 20). Furthermore, a stronger solvent interaction also slowed down drying and removal, which reduced the nucleation rate during recrystallization to promote higher crystallinity (21, 22).

### Grain potential homogenization and electronic structure

UV photoelectron spectroscopy measurements showed that the Oc 2D/3D perovskite created a type I band alignment relative to the bare 3D perovskite (fig. S21). This unfavorable energy offset impeded hole extraction toward spiro-MeOTAD (23, 24). By contrast, the work function and valence band maximum shifts netted a type II alignment for the OcMA:S 2D/3D perovskite and created an energy cascade to bridge hole extraction. OcMA:S and OcMA had similar energetic shifts, consistent with both films having phase-pure 2D ( $n = 2$ ) interlayers, as shown in GIWAXS results. In terms of topographical morphology, no obvious difference was observed between the 2D/3D perovskites in Fig. 2F and fig. S22 from atomic force microscopy (AFM). The surface morphology of the 2D interlayer was not obviously visible in Fig. 2F because the AFM measurement setup was optimized for electrical sensitivity, which sacrificed topography resolution (supplementary text S5). Potential maps measured with Kelvin probe force microscopy (KPFM; Fig. 2G) showed that the bare 3D film had large intragrain and grain-to-grain potential variations caused by abundant surface defects that created localized charging effects (25). The potential profile transformed into a different pattern for the Oc film as a result of 2D interlayer formation, but individual grains were not resolvable because of intragrain potential inhomogeneity. In this case, the

potential fluctuations were caused by the coexistence of multiple phases: unreacted PbI<sub>2</sub>, 2D ( $n = 1$ ), and 2D ( $n = 2$ ). For the OcMA:S film, the intragrain potential uniformity was smoothed out (right, Fig. 2G) by the phase-pure 2D ( $n = 2$ ) interlayer and its long-range structural ordering (i.e., high crystallinity). The AFM morphological grain boundary now corresponded spatially with the KPFM potential boundary, and individual grains were distinguishable because of the homogenized intragrain potential.

Transient reflection spectroscopy (TRS) allowed us to decouple surface versus bulk carrier dynamics in the 3D perovskite by optically generating carriers with short and long wavelengths and modeling the carrier diffusion from the surface (Fig. 2H) (26). For the OcMA:S film, the carriers diffused away from the 2D/3D interface more efficiently. For example, with 3.54-eV excitation light, 50% of photocarriers moved away from the surface within 50 ps for the OcMA:S film, whereas it took 100 ps for the Oc film, consistent with the homogenized surface potential profile and reduced nonradiative recombination. Conversely, by using time-resolved microwave conductivity (TRMC), we found that the carrier lifetime for the OcMA:S film was marginally improved over that for the Oc film (17.7 to 19.0  $\mu$ s, 7.3% increase) (Fig. 2I and fig. S23). Because TRMC is a bulk technique lacking surface sensitivity, these results implied that the 2D perovskite had minimal impact on the bulk 3D perovskite. Direct visualization was obtained by cross-sectional scanning electron microscopy (SEM) imaging, where the 2D perovskite was seen as a conformal layer formed on top of the 3D perovskite (fig. S24). This result was also consistent with time-of-flight secondary ion mass spectrometry (ToF-SIMS) profiling of the elemental distributions (fig. S25). Moreover, the optical bandgap of the 2D/3D perovskites was also comparable (fig. S26). These results suggest that the 2D perovskite was mostly confined to the 3D perovskite surface with no appreciable bulk diffusion.

### Device characterization

We compared the performance of devices based on the 2D/3D perovskites that had the longest carrier lifetimes and found that the PCE increased as bare 3D < Oc < OcMA:F < OcMA:PC < OcMA:S devices (Fig. 3, A and B; fig. S27; and table S7). This trend was primarily due to an increasing open-circuit voltage and fill factor, consistent with the increasing carrier lifetime. 2D phase purity contributed to the improvement when comparing between the Oc device versus the other 2D/3D devices, whereas 2D crystallinity accounted for the differences between the OcMA:S, OcMA:PC, and OcMA:F devices, which were all phase-pure and differed only in crystallinity. Generally, the chemical bath-deposited SnO<sub>2</sub> (CBD-SnO<sub>2</sub>) devices had higher PCE than that of the nanoparticle SnO<sub>2</sub> (NP-SnO<sub>2</sub>) devices (fig. S28). The OcMA:S devices had the best performance overall, with the champion device based on CBD-SnO<sub>2</sub> reaching a PCE of 25.9% with minimal hysteresis (Fig. 3C and table S8).

The device stability was assessed through MPP tracking under full-spectrum 1-sun AM 1.5G illumination (UV included). We emphasize that all devices for all stability tests were of the n-i-p structure based on spiro-MeOTAD. No active cooling or heating was applied, and we measured the actual device temperature to be 40°C to 45°C. The target OcMA:S device (Fig. 3D), with a peak PCE of 24.3%, sustained its performance with minimal degradation and retained 96.4% of its initial PCE after >1700 hours. The control Oc device degraded the most rapidly, dropping to 74.1% of its initial performance after 500 hours. The OcMA:PC and OcMA:F devices had stability intermediate to those of the OcMA:S and Oc devices (fig. S29). Both the OcMA:PC and OcMA:F devices showed the same decay behavior (linear decrease after initial rise for ~75 hours), which was distinct from that of the OcMA:S device.

Comparing the devices with or without excess PbI<sub>2</sub> demonstrated the role of the 2D interlayer. The “Oc no excess” device had no excess PbI<sub>2</sub> in the 3D composition, but its stability and PCE were still far

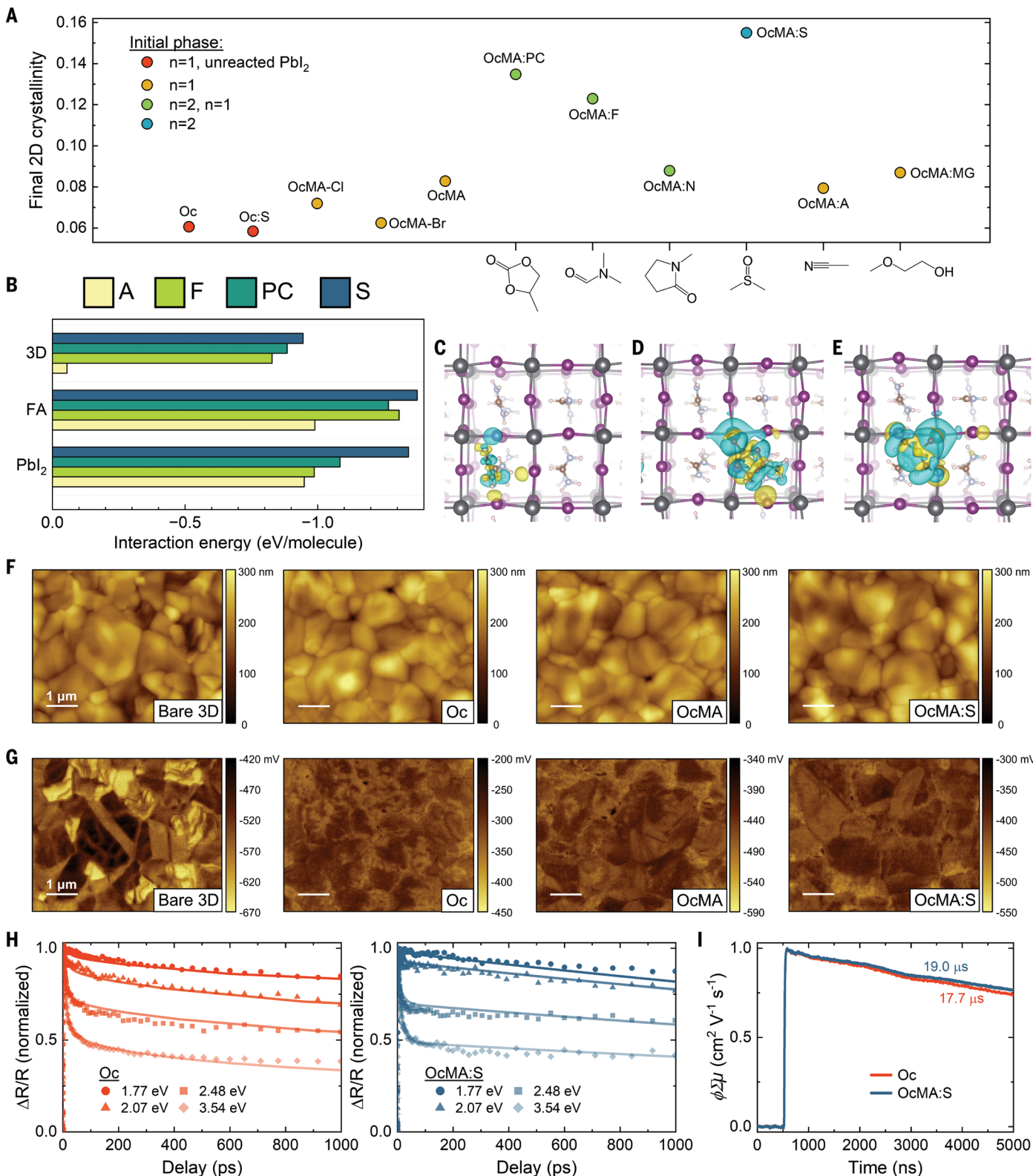


**Fig. 2. Expansion to different 2D fabrication systems, potential uniformity, and carrier dynamics.** (A) Plot of the 2D crystallinity (vertical axis) and the initial phase species (color coded). The 2D crystallinity was quantified by the 2D ( $n = 2$ ):3D integrated area ratio. (B) Interaction energy per solvent molecule with the 3D perovskite surface or 3D perovskite components. (C to E) Slab models of the 3D perovskite surface bonded with acetonitrile (C), propylene carbonate (D), and dimethyl sulfoxide (E). (F and G) AFM topography (F) and KPFM potential mapping (G) of the 2D/3D perovskites. Scale bars, 1  $\mu\text{m}$ . (H) TRS carrier dynamics of the control Oc (left) and target OcMA:S (right) 2D/3D perovskites on glass. The probe energy was 1.53 eV. Solid lines were fitted using a diffusion model. Any decay in the TRS dynamics represents surface carrier dynamics and not recombination, i.e., transient absorption dynamics show no decay in 1000 ps.  $\Delta R/R$ , reflectivity change relative to initial reflectivity. (I) TRMC transients of the control Oc and target OcMA:S 2D/3D perovskites on quartz.  $\phi \Sigma \mu$ , product of the quantum efficiency ( $\phi$ ) of free carrier generation with the sum of electron and hole mobilities ( $\Sigma \mu$ ).

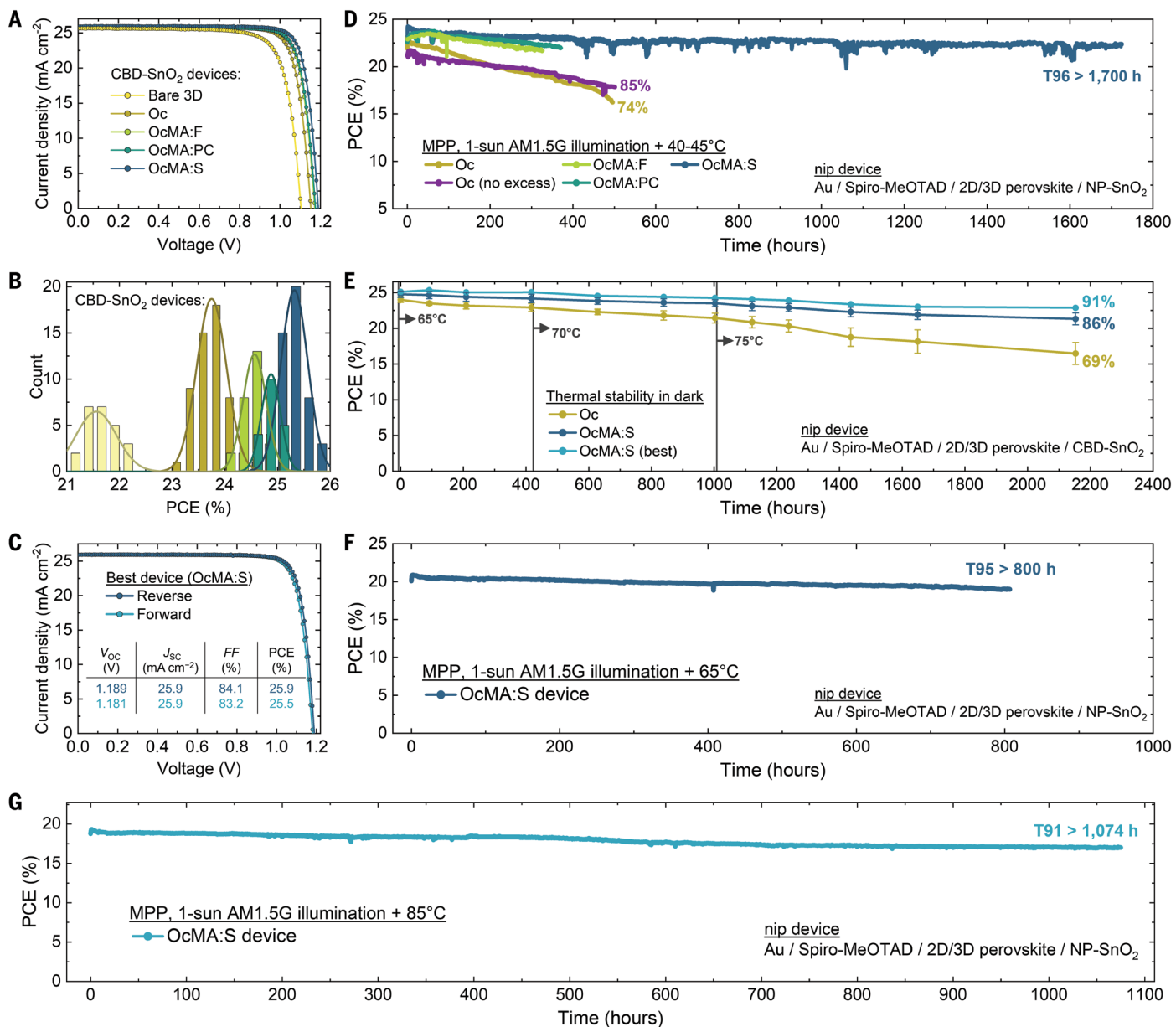


**Fig. 3. Device performance and stability.** (A) Current density-voltage curves of the best devices based on CBD-SnO<sub>2</sub> for the different 2D/3D perovskites. (B) Histogram of the device PCE distribution based on CBD-SnO<sub>2</sub>. (C) Current density-voltage curves of the champion OcMA:S device based on CBD-SnO<sub>2</sub>.  $V_{\text{oc}}$ , open-circuit voltage;  $J_{\text{sc}}$ , short-circuit current density; FF, fill factor. (D) MPP tracking under 1-sun AM1.5G illumination (UV included) of the devices at 40°C to 45°C in a nitrogen atmosphere. T96, time taken for efficiency to degrade to 96% of its initial value. (E) Thermal stability test of the devices in the dark. Error bars represent the standard deviation of eight devices. (F) Sixty-five degrees Celsius MPP tracking of the OcMA:S device under 1-sun AM1.5G illumination (UV included) in a nitrogen atmosphere. (G) Eighty-five degrees Celsius MPP tracking of the OcMA:S device under 1-sun AM1.5G illumination (UV included) in a nitrogen atmosphere.

short of the target OcMA:S device (Fig. 3D). The “OcMA:S no excess” device was more durable than the “Oc no excess” device (fig. S30). Yet, the target OcMA:S device (excess PbI<sub>2</sub> composition but no residual PbI<sub>2</sub> after 2D formation) showed the greatest durability improvement. These comparisons demonstrate the interplay between the 2D interlayer and excess PbI<sub>2</sub> to stabilize the device and simultaneously maintain a high PCE. None of the 2D/3D devices underwent the rapid initial burn-in degradation seen for all the bare 3D devices (fig. S31), so burn-in was not caused by residual PbI<sub>2</sub> (supplementary text S6). The 2D interlayer passivation of defects accounted for the absence of burn-in, which was caused by rapid defect migration (12–14). Additionally, the solvent alone without 2D interlayer formation did not improve stability (fig. S32).

Conventional spiro-MeOTAD is doped with 4-tert-butylpyridine (tBP) and lithium bis(trifluoromethane)sulfonimide (LiTFSI). Such dopants are hygroscopic, highly diffusible, and lower the glass transition temperature of spiro-MeOTAD (27–29), causing a variety of device degradation problems especially at higher temperatures. The spiro-MeOTAD used in this work contained neither tBP nor LiTFSI, which motivated us to assess our devices at elevated temperatures. We first tested the thermal stability in the dark, progressively increasing the temperature from 65°C to 75°C (Fig. 3E). After >2100 hours, on average (eight devices), the OcMA:S devices preserved 86% of their initial PCE. The most stable OcMA:S device retained 91% of its initial performance. We then performed MPP tracking of the OcMA:S device actively heated at 65°C (Fig. 3F). The lower initial PCE was caused by the

negative temperature coefficient of PSCs, consistent with literature reports of  $-0.15\%$  per degree Celsius (30, 31). The device retained 95% of its initial PCE after  $>800$  hours. We further increased the heating temperature to  $85^\circ\text{C}$  under 1-sun AM 1.5G illumination (UV included). This n-i-p device based on our spiro-MeOTAD retained 91% of its initial performance after 1074 hours of illumination (Fig. 3G). All devices in this work were of the n-i-p structure based on spiro-MeOTAD, which generally have poorer stability than their inverted p-i-n counterparts (29, 32). Especially at higher temperatures, fewer n-i-p devices have been reported. We demonstrate durable n-i-p devices, competitive with state-of-the-art inverted p-i-n devices (table S9).

### A robust 2D interlayer

The control Oc device lost most of its 2D interlayer under illumination, whereas the bare 3D perovskite under illumination did not undergo any sort of decomposition (fig. S33). Thus, problems with the 2D interlayer limited the overall durability of the 2D/3D Oc device. For the target OcMA:S device, the 2D ( $n = 2$ ) phase was in a stable state both structurally (crystalline long-range ordering) and thermodynamically (spontaneously formed single phase). The 2D interlayer was still intact after  $>2500$  hours illumination without any sort of phase transformation (Fig. 4A and fig. S34). Long-term retention of this robust 2D interlayer was key to stabilizing the device. During aging, the 2D

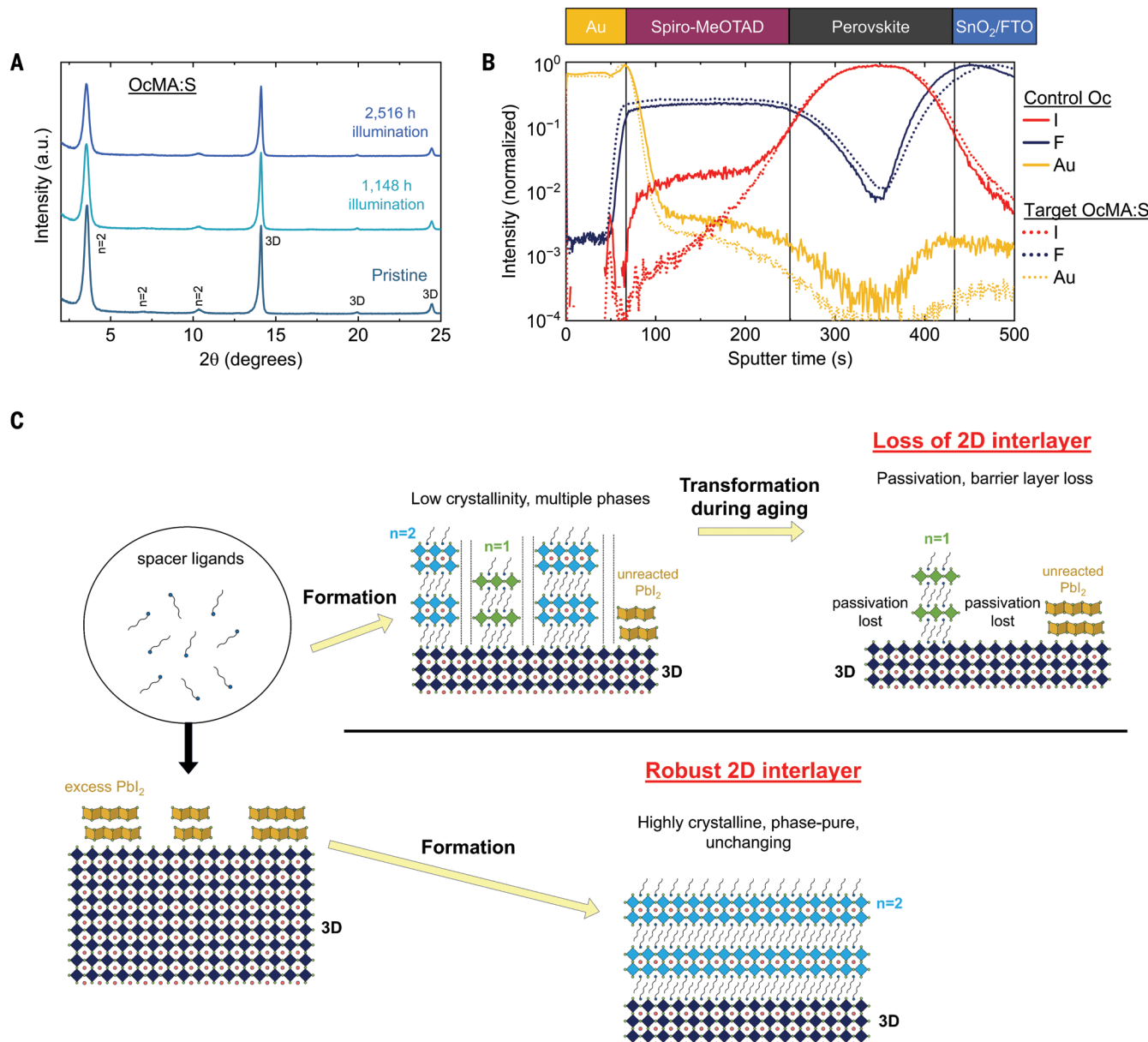


**Fig. 4. Evolution of 2D perovskite interlayers.** (A) XRD patterns of the target OcMA:S 2D/3D perovskite aged under 1-sun AM 1.5G illumination under open-circuit condition in a nitrogen glovebox. The XRD was performed on devices of structure spiro-MeOTAD/2D perovskite/3D perovskite/SnO<sub>2</sub>/fluorine-doped tin oxide (FTO). The 2D perovskite was thus buried under the spiro-MeOTAD layer for these measurements. (B) Postmortem ToF-SIMS elemental depth profiling of the devices of structure Au/spiro-MeOTAD/2D perovskite/3D perovskite/SnO<sub>2</sub>/FTO. The devices were aged simultaneously together for 528 hours under 1-sun AM 1.5G illumination under open-circuit condition in a nitrogen glovebox. Note that the fluorine signal marks either the spiro-MeOTAD layer or FTO substrate layer. The former corresponds to the TFSI<sup>-</sup> counteranion in spiro(TFSI)<sub>2</sub>. (C) Schematic illustrating the formation and transformation of 2D perovskite interlayers, representing the Oc (top) and OcMA:S (bottom) 2D/3D perovskites.

interlayer passivated defects and suppressed ion migration, functioning like a blocking barrier. When the 2D perovskite degraded, ions penetrated into the transport layer unimpeded, as observed through postmortem analysis of the aged devices (Fig. 4B).

Initially phase-pure 2D interlayers could degrade differently. For both the OcMA:PC and OcMA:F devices, although the pristine 2D perovskite was phase-pure 2D ( $n = 2$ ), it transformed into the 2D ( $n = 1$ ) phase (fig. S35). Nevertheless, further decomposition into PbI<sub>2</sub> did not occur, unlike with the control Oc device. We further attempted to generalize our results. For the “Oc no excess” device (fig. S36), a phase-pure 2D ( $n = 2$ ) perovskite transformed into 2D ( $n = 1$ ) under illumination, so the 2D interlayer transformation was not caused by excess PbI<sub>2</sub>. By contrast, the “OcMA:S no excess” device (fig. S37) was durable under the same conditions, so our method worked without excess PbI<sub>2</sub>. Our strategy also worked on alternative 2D interlayers based on different widely used spacer organic ligands (fig. S38 and S39). This work showcases the importance of attaining a robust 2D interlayer (Fig. 4C).

## REFERENCES AND NOTES

1. F. Zhang et al., *Science* **375**, 71–76 (2022).
2. J. Tong et al., *Nat. Energy* **7**, 642–651 (2022).
3. R. Azmi et al., *Science* **376**, 73–77 (2022).
4. S. Sidhik et al., *Science* **377**, 1425–1430 (2022).
5. C. Liu et al., *Nature* **633**, 359–364 (2024).
6. R. Lin et al., *Nature* **603**, 73–78 (2022).
7. Z. Liang et al., *Nature* **624**, 557–563 (2023).
8. R. Azmi et al., *Nature* **628**, 93–98 (2024).
9. H. Gu et al., *Nat. Rev. Mater.* **8**, 533–551 (2023).
10. M. Kim et al., *Joule* **3**, 2179–2192 (2019).
11. J.-W. Lee, S. Tan, S. I. Seok, Y. Yang, N.-G. Park, *Science* **375**, eabj1186 (2022).
12. K. Domanski et al., *Energy Environ. Sci.* **10**, 604–613 (2017).
13. J. M. Azpiroz, E. Mosconi, J. Bisquert, F. De Angelis, *Energy Environ. Sci.* **8**, 2118–2127 (2015).
14. S. Tan et al., *Adv. Mater.* **32**, e1906995 (2020).
15. Q. Chen et al., *Nano Lett.* **14**, 4158–4163 (2014).
16. A. H. Proppe et al., *Nat. Commun.* **12**, 3472 (2021).
17. S. Tan et al., *J. Am. Chem. Soc.* **143**, 6781–6786 (2021).
18. J. Xue et al., *J. Am. Chem. Soc.* **141**, 13948–13953 (2019).
19. J. Park et al., *Nature* **616**, 724–730 (2023).
20. H. Lu et al., *Science* **370**, eabb8985 (2020).
21. Y. Xu, M. Wang, Y. Lei, Z. Ci, Z. Jin, *Adv. Energy Mater.* **10**, 2002558 (2020).
22. J.-W. Lee, H.-S. Kim, N.-G. Park, *Acc. Chem. Res.* **49**, 311–319 (2016).
23. J. Euvrard, Y. Yan, D. B. Mitzi, *Nat. Rev. Mater.* **6**, 531–549 (2021).
24. J. Peng et al., *Nature* **601**, 573–578 (2022).
25. Q. Jiang et al., *Nature* **611**, 278–283 (2022).
26. Y. Yang et al., *Nat. Energy* **2**, 16207 (2017).
27. T. Malinauskas et al., *ACS Appl. Mater. Interfaces* **7**, 11107–11116 (2015).
28. F. Lamberti et al., *Chem* **5**, 1806–1817 (2019).
29. F. M. Rombach, S. A. Haque, T. J. Macdonald, *Energy Environ. Sci.* **14**, 5161–5190 (2021).

30. T. Moot et al., *ACS Energy Lett.* **6**, 2038–2047 (2021).

31. S. M. Park et al., *Nature* **624**, 289–294 (2023).

32. M. V. Khenkin et al., *Nat. Energy* **5**, 35–49 (2020).

## ACKNOWLEDGMENTS

This work was performed in part in the MIT.nano Characterization facilities. We thank C. Moorman for the field-emission SEM measurements. The authors thank J. Cox and C. Settens for assisting with the XRD measurements. The US government retains a nonexclusive, paid-up, irrevocable, worldwide license to publish or reproduce the published form of this work or allow others to do so for US government purposes, and the publisher, by accepting the article for publication, acknowledges this. **Funding:** S.T. was initially supported by First Solar, Inc., during the early stages of the project and then was supported by the US Department of Energy (DOE) Office of Energy Efficiency and Renewable Energy (EERE) under the Solar Energy Technologies Office under award no. DE-EE0009512. M.-C.S. and Y.L. were supported by the US DOE Office of EERE under the Solar Energy Technologies Office under award no. DE-EE0009512. M.J.G. was supported by First Solar, Inc. T.K. acknowledges support by the US DOE Office of Science, Office of Basic Energy Sciences, Materials Sciences and Engineering Division, under contract no. DE-AC02-05-CH11231 (D2S2 program KCD2S2). Part of the work was carried out as a user project at the Molecular Foundry, a user facility supported by the US DOE Office of Science, Office of Basic Energy Sciences, under contract no. DE-AC02-05CH11231. Work at the Advanced Light Source (ALS) was done at beamline 12.3.2. The ALS is a DOE Office of Science User Facility under contract no. DE-AC02-05CH11231. J.-W.L. acknowledges support by a National Research Foundation of Korea (NRF) grant funded by the Korean government (Ministry of Science and ICT) under contract no. RS-2024-00416154. N.-G.P. acknowledges financial support from the NRF grant funded by the Korean government (Ministry of Science and ICT) under contract no. NRF-2021R1A3B1076723 (Research Leader Program). Computing resources used in this work were provided by the National Center for High Performance Computing of Turkey (UHeM). Transient reflection (TR), transient absorption (TA), and time-resolved microwave conductivity (TRMC) spectroscopy studies were supported from the Center for Hybrid Organic-Inorganic Semiconductors for Energy (CHOISE), an Energy Frontier Research Center funded by the Office of Basic Energy Sciences, Office of Science, within the US DOE. **Author contributions:** S.T. conceived the idea. S.T. and M.-C.S. designed and conducted most of the experiments, supervised by M.G.B. S.T., M.-C.S., and Y.L. performed the GIWAXS and XRD measurements. T.K. assisted with the GIWAXS measurements and analyses, supervised by C. M.S.-F. Y.-K.L. assisted with the XRD measurements. Y.D. performed the TA and TR measurements, supervised by M.C.B. and K.Z. M.C.B. analyzed and developed the model for the TA and TR results. B.W.L. and S.Y.P. performed the TRMC measurements and analyses, supervised by K.Z. S.-G.C. and J.-H.L. performed the KPFM and AFM measurements and analyses, supervised by N.-G.P. and J.-W.L. S.-G.C. did the ToF-SIMS measurements and analyses, supervised by J.-W.L. I.Y. did the theoretical calculations and analyses. R.Z., M.J.G., and H.Z. assisted with experiments and provided valuable discussions. S.T., M.-C.S., K.Z., and M.G.B. wrote the first manuscript draft. All authors contributed feedback and commented on the manuscript. **Competing interests:** S.T., M.-C.S., and M.G.B. are inventors of a provisional patent (US 63/662,739) related to the subject matter of this manuscript. The other authors declare that they have no competing interests. **Data and materials availability:** All data needed to evaluate the conclusions in the paper are present in the paper or the supplementary materials. **License information:** Copyright © 2025 the authors, some rights reserved; exclusive licensee American Association for the Advancement of Science. No claim to original US government works. <https://www.science.org/about/science-licenses-journal-article-reuse>

## SUPPLEMENTARY MATERIALS

[science.org/doi/10.1126/science.adr1334](https://science.org/doi/10.1126/science.adr1334)

Materials and Methods; Supplementary Text S1 to S6; Figs. S1 to S39; Tables S1 to S8; References (33–65)

Submitted 17 June 2024; resubmitted 31 October 2024; accepted 18 March 2025

10.1126/science.adr1334